Electrochimica Acta 400 (2021) 139414

Contents lists available at ScienceDirect

Electrochimica Acta

journal homepage: www.elsevier.com/locate/electacta

Electrochemical performance of manganese hexacyanoferrate cathode material in aqueous Zn-ion battery

Min Li[a], Rosalinda Sciacca[b], Mariam Maisuradze[a], Giuliana Aquilanti[c], Jasper Plaisier[c], Mario Berrettoni[d], Marco Giorgetti[a,*]

[a] Department of Industrial Chemistry "Toso Montanari", University of Bologna, Viale del Risorgimento 4, Bologna 40136, Italy
[b] Department of Industrial Chemistry "Toso Montanari", University of Bologna, UOS Campus Di Rimini, via dei Mille 39, Rimini 47921, Italy
[c] Elettra-Sincrotrone Trieste, s.s. 14, km 163.5, Basovizza, Trieste 34149, Italy
[d] School of Science and Technology, Chemistry Division, University of Camerino, Camerino, Italy

ARTICLE INFO

Article history:
Received 8 August 2021
Revised 8 October 2021
Accepted 9 October 2021
Available online 20 October 2021

Keywords:
Sodium manganese hexacyanoferrate
Aqueous Zn-ion battery
Mn/Fe-site study
Ex-situ XAS spectra

ABSTRACT

Manganese hexacyanoferrate (MnHCF) has attracted much attention as promising cathode material for Li and Na ion batteries, owning to its low cost, environmental friendliness, high specific capacity and voltage plateau. Here, the electrochemical performance and electronic structure information of MnHCF were studied in aqueous Zn-ion batteries (ZIBs). Based on the cyclic voltammetry and galvanostatic charge/discharge results, an activation of Fe-sites during beginning cycles was observed, and the capacity contribution of Fe-sites increases from 30 to 86% at C/20 during the first 10 cycles. The local geometric and electronic structure information of MnHCF was investigated by X-ray absorption spectroscopy (XAS) in a set of ex-situ electrodes. From Fe K-edge spectra, it shows a consistent oxidation and reduced state in charged and discharged electrodes, and this indicates that there is no apparent change for the local Fe-sites environment. However, the XAS spectra of Mn K-edge show apparent change after 10 cycles. Compared to the rhombohedral phase of Zinc hexacyanoferrate (ZnHCF), a -Zn-CN-Fe- structural framework was detected in the cycled MnHCF samples, and this indicates that a part of Zn replaced Mn-sites, because of the dissolution of the Mn-sites. The gradual activation of Fe-sites at the beginning cycles can be attributed to the alleviation spatial resistance with the dissolution of Mn-sites, and the replacement of Zn for Mn explains the decreasing capacity during cycling.

1. Introduction

Aqueous rechargeable metal-ion batteries (ARMBs) have giant potential in large-scale energy storage due to the advantages of low cost, safety, environmental benign and high ionic conductivity. To date, a variety of ARMBs based on many metal ions including naturally-abundant alkali metal ions (Na^+ and K^+) [1–4] and multivalent charge carriers (Zn^{2+}, Mg^{2+}, Al^{3+}, etc.) have been investigated [5–9]. Among different ARMBs, aqueous Zinc-ion batteries (ZIBs) are considered as some of the most promising candidates for stationary application, because of the unique properties of metallic zinc, which is an ideal anode material with high theoretical gravimetric and volumetric capacity of 820 mAh g^{-1} and 5855 mAh cm^{-3}, low electrochemical potential (−0.76 V vs. SHE), high abundance and intrinsic safety [10,11]. Meanwhile, the stripping-plating of Zn metal anode also shows good reversibility in mildly acidic aqueous solutions [12].

Among different cathode materials, Prussian blue analogues (PBAs) as bimetallic cyanides are considered as promising cathode material for Zn-ion batteries, due to their large ionic channels and interstices in the lattice, abundant redox-active sites, and strong structural stability [13,14]. Copper hexacyanoferrate (CuHCF) and Zinc hexacyanoferrate (ZnHCF) were first investigated as cathode material in aqueous ZIBs by Jia et al. [15] and Zhang et al. [16], and they found that unlike manganese-based and vanadium-based materials, [6,17–19] CuHCF and ZnHCF exhibited high operation voltage, which can reach 1.7 V. Manganese hexacyanoferrate (MnHCF) [20–22], Cobalt hexacyanoferrate (CoHCF) [23] and Vanadium hexacyanoferrate (VHCF) [24] have also been used as cathode materials for aqueous ZIBs, and they do not only show a high discharge potential (> 1.5 V), but also a large-capacity due to the multi-redox active sites. However, most of PBAs are facing the problem of capacity fading and short cycle lifespan during the Zn-ions insertion and extraction in aqueous electrolyte. La Mantia and coworkers [25–27] have reported a series of works about the structural

* Corresponding author.
E-mail address: marco.giorgetti@unibo.it (M. Giorgetti).

https://doi.org/10.1016/j.electacta.2021.139414
0013-4686/

and phase change of CuHCF during Zinc-ion insertion. They found a new secondary phase was formed during insertion/extraction of Zn^{2+} based on XRD data, but which are not well matched with the already reported orthorhombic or monoclinic ZnHCF phases, and they proposed that the structural changes can be related to the insertion of zinc-ions into the interstitial site and/or replacement of Cu sites due to the dissolution of Cu^{2+}. Renman and coworkers [28] studied the crystal structure changes of CuHCF by using operando synchrotron X-ray diffraction (XRD). They found that the Zn^{2+}occupy both $Fe(CN)_6$ vacancy site (4a) and the cavity (8c), and during the discharge process, the change of occupancy for the 4a site (increasing) and the 8c site (decreasing) is quite opposite. They proposed that the structural changes are associated with swapping of Zn^{2+} between the tunnels and the vacant $Fe(CN)_6$ sites. Thus, understanding the crystal distortion and phase transformation of the electrode material can well explain the capacity fading problems during cycling. However, determining exactly where Zn^{2+} resides within the cavities/channels is not a straightforward task.

In this paper, the synthesis ofMnHCF is described, as well as its application as cathode material for ZIBs, in comparison with the other PBAs. MnHCF is composed of only highly abundant metals and displays large capacity and high discharge potential [29]. X-ray absorption spectroscopy (XAS) was used to study the electrochemical-structural and electronic properties of MnHCF in aqueous ZIBs. As XAS is a powerful tool that can be tuned to a chosen element,the physiochemical properties and the local geometric and /or electronic structure of the selected element can be obtained. Here, ex-situ XAS was used to record Mn, Fe and Zn k-edge spectra at different charge and discharge states. By tracing the electron structural changes, we can get information about local metal structural modifications during Zn^{2+}insertion and release.

2. Experimental

2.1. Synthesis of MnHCF and ZnHCF

The synthesis of MnHCF was based on a simple and reproducible co-precipitation method, as reported in ref [29]. 100 ml 0.1 M manganese sulfate monohydrate ($MnSO_4 \bullet H_2O$) solution and 100 ml 0.1 M sodium ferrocyanide decahydrate ($Na_4Fe(CN)_6 \bullet 10H_2O$) simultaneously added dropwise to an aqueous solution of sodium sulfate (Na_2SO_4, 0.1 M 100 mL) by using a peristaltic pump at a rate of 4 mL min^{-1}. Both reagents and reaction batch were kept under N_2 atmosphere at constant temperature (40 ± 2 °C) using a water bath. The obtained solution was aged for 5 days, assuring complete decantation. Then the precipitate was collected via centrifugation at 4000 rpm and washed three times with distilled water, dried at 60 °C for 48 h.

ZnHCF was also synthesized by a co-precipitation method: 25 mM $ZnCl_2$ solution added dropwise to a 25 mM $K_3Fe(CN)_6$ solution with stirring. A yellowish colloidal solution was obtained and it was left standing overnight. The precipitated sample was washed with deionized water and centrifuged several times in order to remove the unreacted salts and separate the solid products. The precipitate was dried at 80 °C overnight.

2.2. Electrode preparation and electrochemical tests

The electrochemical properties of the obtained material were evaluated in three-electrode mode: the active material as working electrode, zinc sheet as reference electrode and counter electrode. The working electrode was prepared by mixing the active material (70%), super C65 (25%) and PTFE (5%) and grinding until we got homogenous thin solid slice. Then we used a puncher to get 8 mm (diameter) pellets with a mass density of around 5∼10 mg/cm^2, then an aluminum mesh was used to fix the pellet. Full coin cells were assembled by using metal Zn sheet as anode and MnHCF and ZnHCF pellet as cathode in 3 M $ZnSO_4$ electrolyte.

Cyclic voltammetry (CV) was performed by means of CHInstruments Model 660. The CV test was conducted in potential range 1∼2.2 V (three-electrode) and 1,2 V (coin cell) vs Zn^{2+}/Zn in 3 M $ZnSO_4$ aqueous solution.

Galvanostatic cycling with potential limit (GCPL) was conducted in 1< E <1.9 V vs Zn^{2+}/Zn potential window at different current densities. Cycling started after a rest time (3 h) at OCP condition with a positive imposed current.

2.3. Characterization

A Microwave plasma-atomic emission spectrometer (MP-AES) 4210 was used to detect the composition of the active material. During the test, three different wavelengths were chosen for each element.

Infrared (IR) spectrum was measured using a Bruker Alpha FT-IR spectrometer in ATR (Attenuated Total Reflectance) mode at a spectral range of 4000–400 cm^{-1}.

Thermogravimetric analysis (TGA) was performed in air atmosphere from room temperature to 500 °C, with a heating rate of 5 °C min^{-1}, and rapid cooling.

Powder X-ray diffraction (PXRD) data were recorded by using a monochromatic X-ray beam (wavelength of 1 Å) at the MCX beamline in ELETTRA synchrotron Trieste (Italy) [30]. Data were collected in a capillary geometry, setting the spinner at 180 rpm. The X-ray diffraction pattern was collected consecutively in the range 5°< 2θ< 70°, with steps of 0.01° and an acquisition time of 1 s/step. The crystal structure was refined using Fullprof Suite [31].

X-ray absorption spectroscopy (XAS) experiments were conducted at Elettra Synchrotron Trieste (Italy), at XAFS beamline [32]. The storage ring was operated at 2.0 GeV in top-up mode with a typical current of 300 mA. Data were recorded at the Fe, Mn and Zn K-edge in transmission mode using ionization chambers filled with a mixture of Ar, N_2, and He to have 10, 70, and 95% of absorption in the I_0, I_1 and I_2 chambers, respectively. An internal reference of iron, manganese and zinc foil was used for energy calibration in each scan. This allowed a continuous monitoring of the energy during consecutive scans. The white beam was monochromatized using a fixed exit monochromator equipped with a pair of Si (111) crystals. Spectra were collected with a constant k-step of 0.3 nm^{-1} with 3 s per point acquisition time from 6345 to 7100 eV, from 6920 to 8350 eV, and from 9467 to 10,897 eV around Mn, Fe and Zn K-edges, respectively. XAS spectra were calibrated using the Athena program [33].

3. Result and discussion

The X-ray powder diffraction (XRPD) pattern of MnHCF is shown in Fig. 1(a). Rietveld refinement was carried out to refine the lattice parameters and atomic positions and the result showed that MnHCF has a monoclinic lattice (space group: $P2_1/n$) with a, b, c and β equal to 10.571(6) Å, 7.463 (9) Å, 7.406 (9) Å and 92.10(8), respectively. IR spectroscopy of MnHCF is shown in Fig. 1(b). Two small sharp peaks occur around 3604 and 3532 cm^{-1}, which can be attributed to -O-H stretching mode arising from surface water (non/weak-hydrogen bonded) and interstitial water. Meanwhile, the peak at 1620 cm^{-1} is related to the bending mode of the -O-H group of interstitial water. A distinguishable peak appears at around 2065 cm^{-1}∼ 2075 cm^{-1}, which is the characteristic peak of the -C≡N group. Because the cyanide bridge is extremely sensitive to its environment and oxidation states, the wavenumber of -C≡N group here should represent the Mn^{II}-C≡N-Fe^{II} group [34,35]. Thermogravimetric analysis (TGA) of the prepared sample

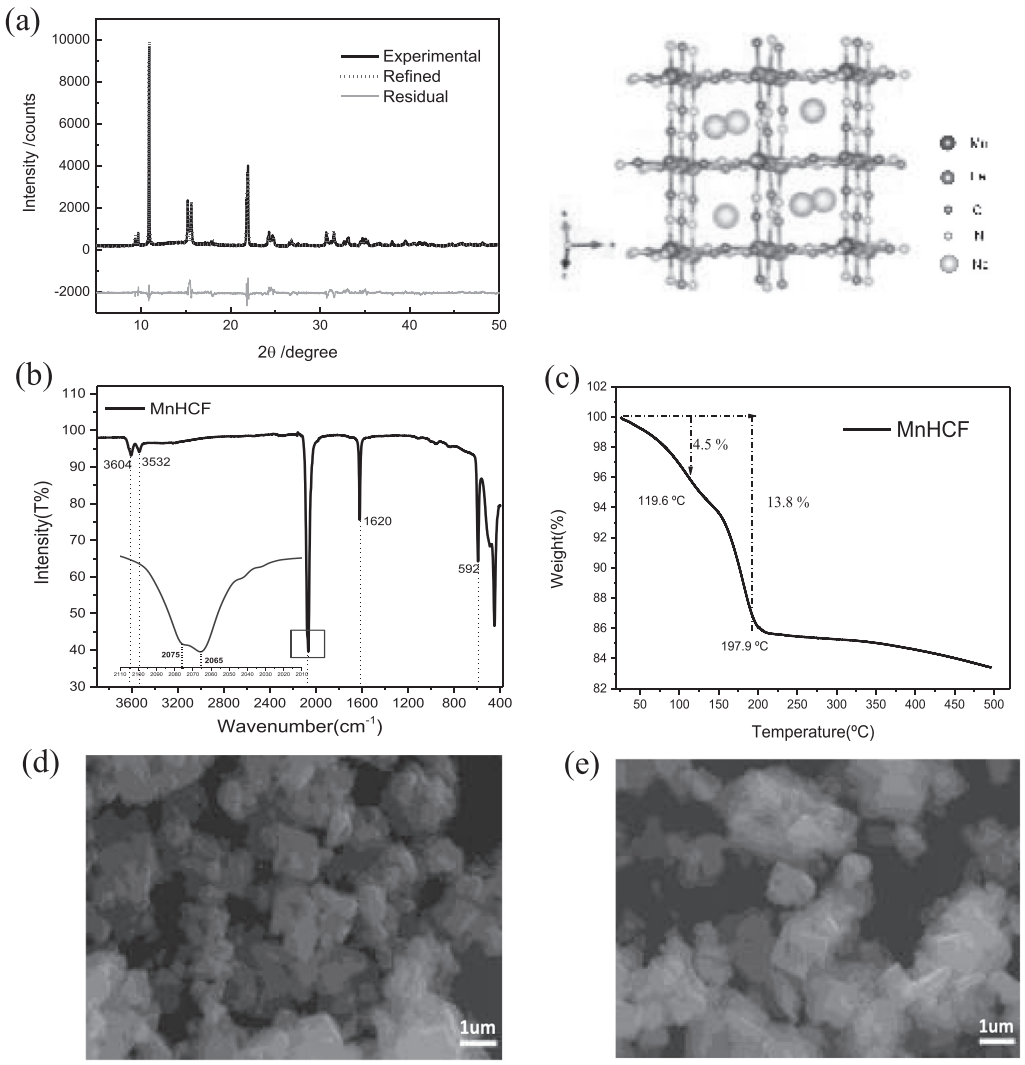

Fig. 1. (a) XRPD pattern and Rietveld refinement on MnHCF powder with tridimensional ball and stick structure (right); (b) IR spectrum of MnHCF; (c) TGA curve of MnHCF; (d, e) SEM image of the as-prepared MnHCF.

shows two distinct weight-loss events at around 120 °C and 200 °C (Fig. 1(c)), which are ascribed to the loss of absorbed water and interstitial/structural water, respectively, around 13.8% of the total weight. Combining this with the composition results obtained from ICP-OES measurement (Table S1), the chemical formulation of Mn-HCF is $Na_{1.47}$ Mn [Fe (CN) $_6]_{0.88}$ 2 $6H_2O$. The morphology of the material was studied by scanning electron microscope (SEM), as shown in Fig. 1(d, e). It can be seen that some cubic-shaped particles are distributed in the range of 100–1000 nm.

Electrochemical reversibility and stability of as-prepared Mn-HCF and metal Zn anode were first investigated in a three-electrode system in 3 M $ZnSO_4$ aqueous electrolyte, in which Zn sheet was used as both counter and reference electrode, as shown in Fig. 2(a). In the case of Zn anode (Fig. 2(b)), there is one apparent oxidation peak around 0.16 V (vs. Zn^{2+}/Zn), which is attributed to the dissolution of zinc (stripping). The intensity of the reduction peak of Zn^{2+} keeps increasing along with the negative shift in the potential below 0 V (vs. Zn^{2+}/Zn), which is ascribed to the deposition of zinc on the electrode (plating). Here, Zinc metal anode shows good stripping-plating reversibility in 3 M $ZnSO_4$ electrolyte. CV curves of MnHCF are shown in Fig. 2(c), two oxidation peaks are observed at around 1.62 V and 1.95 V, and one wide reduction peak is at around 1.6 V, which can attributed to the redox couple of the low-spin Fe^{2+}/Fe^{3+} and high-spin Mn^{2+}/Mn^{3+}, respectively [20,36]. Current intensity of cathode redox peaks is increasing with cycles going, and it is probably due to the gradual activation of the electrode. The same phenomenon was also reported for MnO_2 and $ZnMn_2O_4$ [37,38].

Full-cells were assembled by using metal Zn sheet as anode and MnHCF as cathode in 3 M $ZnSO_4$ electrolyte. CV profiles were obtained at different scan rates from 2 to 0.2 mV/s. With decreasing scan rate, a gradual change of redox peaks was observed, both in current intensity and peak position. As shown in Fig. 3(a), two pairs of redox peaks were observed at 1.83/1.50 V and 1.96/1.88 V at the first cycle of 2 mV/s, that becomes progressively one wide anode peak at 1.80 V and two cathode peaks at 1.33 and 1.50 V, as observed at the 5th cycle. When the scan rate decreases to 1 mV/s, two pairs of redox peaks were observed at 1.65/1.48 and 1.80/1.70 V at 5th cycle. As the scan rate reduces to 0.5 and 0.2 mV/s, only one anode peak appeared at around 1.63 V, but two new cathode peaks were observed at 1.26 and 1.39 V, and the peak at around 1.56 V gradually disappeared. Similar to the three-electrode system, current intensity of redox peaks was increasing with the number of cycles at 0.2 mV/s.

In order to trace the change of CV curves at the same current density, a new MnHCF full cell was tested at a scan rate of 0.2 mV/s for 10 cycles. As shown in Fig. 4 (a, b), the CV profile in the first cycle is slightly different from the following ones. The

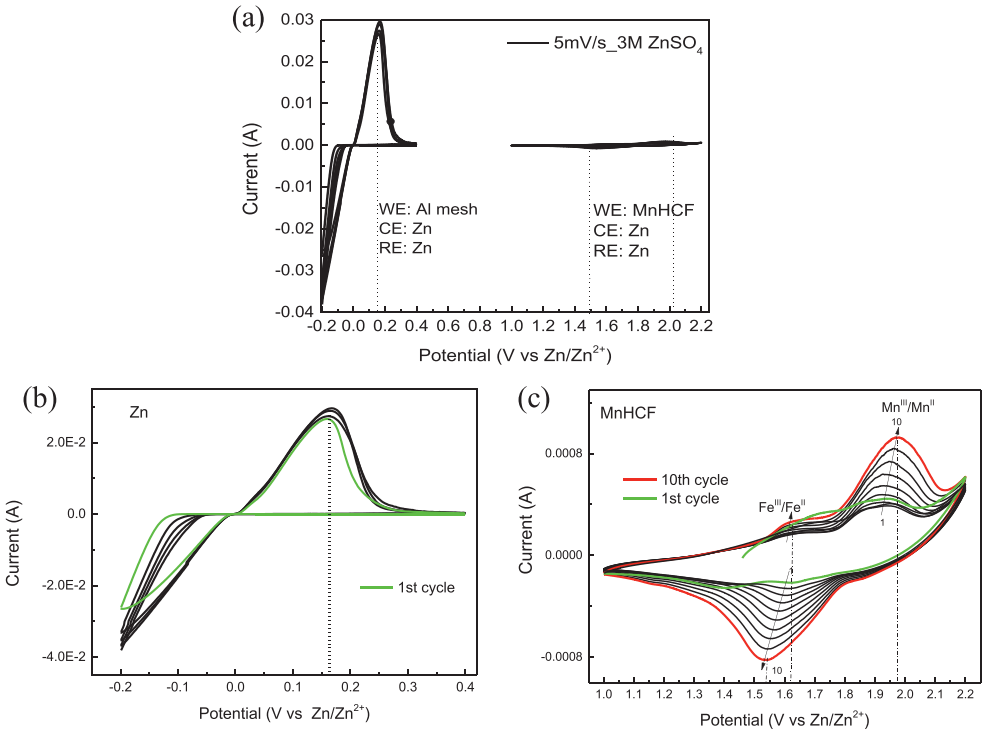

Fig. 2. (a) CV curves of MnHCF and Zn plating/stripping at scan rate of 5 mV s^{-1} in 3 M $ZnSO_4$ electrolyte; (b) zoom-in CV curve of Zn plating/stripping; (c) zoom-in CV curve of MnHCF.

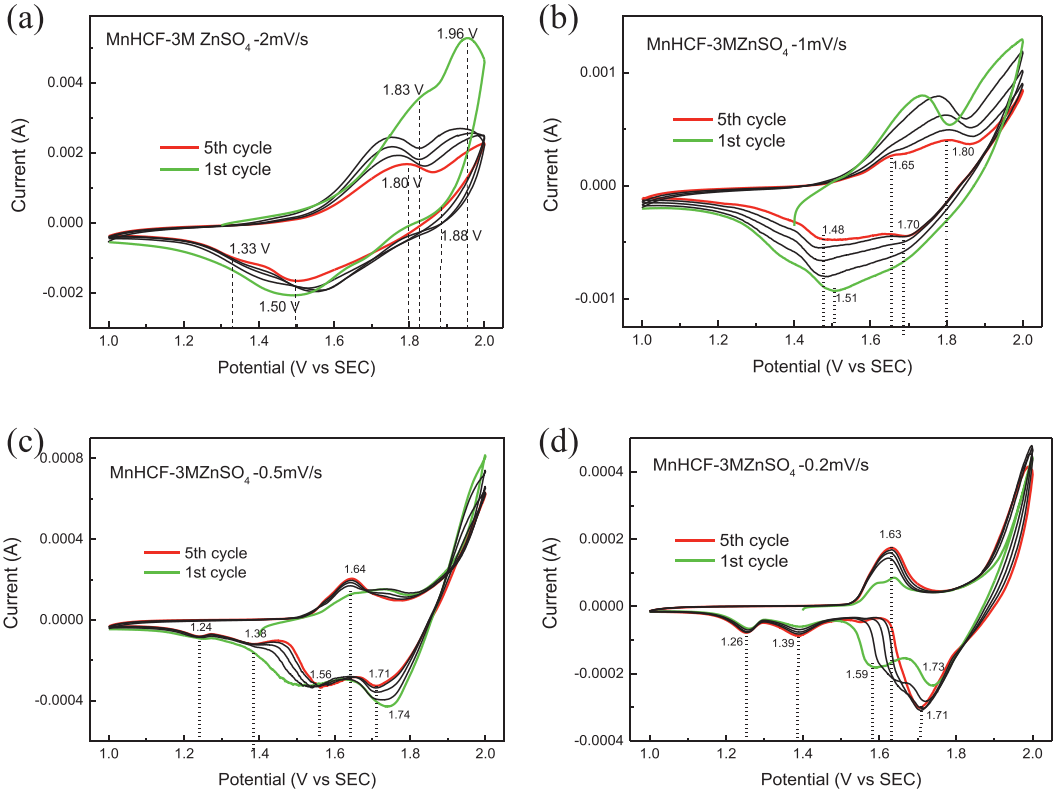

Fig. 3. CV curves of MnHCF full-cell at different scan rate: (a) 2 mV s^{-1}, (b) 1 mV s^{-1}, (c) 0.5 mV s^{-1} and (d) 0.2 mV s^{-1}.

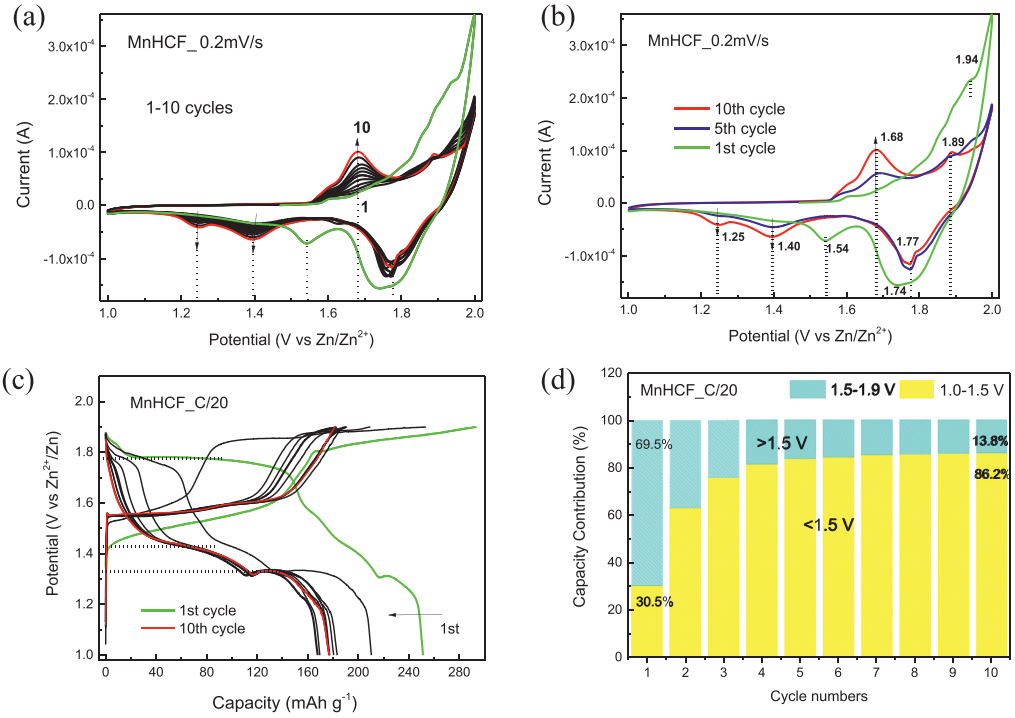

Fig. 4. (a) CV curves of MnHCF full-cell at 0.2 mVs^{-1} for 10 cycles; (b) 1st, 5th and 10th cycle CV curves at 0.2 mVs^{-1}; (c) first 10 cycles of Galvanostatic charge/discharge curves of MnHCF at C/20; (d) the corresponding discharge capacity contribution of different voltage range at C/20.

oxidation peak at 1.94 V can be related to the extraction of Na^+ from electrode during the first charge process (Eq. (1)), while the two reduction peaks at 1.74 V and 1.54 V during the first discharge process can be attributed to the insertion of Zn^{2+} and Na^+ (Eq. (2)), respectively. Two oxidation peaks at 1.68 V and 1.89 V were observed in the successive cycles, which might correspond to Zn-extraction from MnHCF cathode as the Fe^{II} and Mn^{II} states undergo oxidation to the Fe^{III} and Mn^{III} states. Furthermore, except for the reduction peak at 1.77 V, two new reduction peaks at 1.40 and 1.25 V appeared, and in light of the literature reports [21,39], they can be attributed to the reduction of Fe^{3+} to Fe^{2+}. The current intensity of these two peaks was increasing cycle by cycle, as well as the oxidation peak at 1.68 V. This behavior was maybe related to the gradual activation of the electrode and/or the structural transition with insertion/extraction of Zn-ions.

$$Na_{1.47}\,Mn^{II}\left[\,Fe^{II}(CN)_6\right]_{0.88} - xNa^+ - e^- \rightarrow Na_{1.47-x}\,Mn^{III}\left[\,Fe^{III}(CN)_6\right]_{0.88} \quad (1)$$

$$Na_{1.47-x}\,Mn^{III}\left[\,Fe^{III}(CN)_6\right]_{0.88} + yNa^+ + zZn^{2+} + e^- \rightarrow Na_{1.47-x+y}\,zZn\,Mn^{II}\left[\,Fe^{II}(CN)_6\right]_{0.88} \quad (2)$$

The Zn/MnHCF cell was fabricated under open-air conditions, and displayed an open-circuit potential (OCP) around 1.30 V. Fig. 4(c) shows the first 10 charge/discharge profiles of MnHCF in the potential range of 1.0–1.9 V vs. Zn^{2+}/Zn at C/20 rate. The first two charges and discharges of MnHCF showed capacity above 200 $mAhg^{-1}$, and this maybe because of the partial decomposition of electrolyte and extraction/insertion of both Na^+ and Zn^{2+} at the same time. From the third cycle, the discharge capacity was centered at around 176 $mAhg^{-1}$, and the discharge plateaus were also changed with cycling. A discharge plateau at around 1.78 V was initially observed, and then it disappeared gradually. Meanwhile, two new discharge plateaus around 1.42 and 1.33 V have shown up, which are consistent with the CV peaks (Fig. 4(a)). Based on the reduction peaks potential, we calculated the capacity contribution at different voltage range, as shown in Fig. 4(d). The total discharge capacity during the whole cycling process is divided into two main contributions: 1.0–1.5 V and 1.5–1.9 V, which are attributed to the $Fe^{2+/3+}$and $Mn^{2+/3+}$ redox couples, respectively. The capacity contribution of $Fe^{2+/3+}$ increases from 30% at the beginning to 86% at 10th cycle, which is consistent with the CV data where current intensity of $Fe^{2+/3+}$ increases with cycles. Thus, we postulate that there is an activation of Fe-sites within MnHCF structure during Zn-ions insertion/extraction. Meanwhile, the Mn-sites experience a deactivating process and which is probably due to the dissolution of Mn-sites or the change of local environment of Mn-sites, which are discussed later.

The electrochemical performance of an electrode material is derived from the combination of structures, electronic properties and the reversible evolution of active-sites upon the charge and discharge process. In order to detect the change of the structure and the electronic properties of the active-sites inside MnHCF during cycling, ex-situ XAS spectra were recorded at the Fe, Mn and Zn K-edge at different charge and discharge states, as represented by the scheme in Fig. 5. Fe K-edge spectra were recorded at D1, C2 and D10 states, and the pre-edge and k^2-weighted EXAFS signal as well as the corresponding FTs are shown in Fig. 6 (b–d). As expected, in Fig. 6(a) the C2 sample shows an oxidized state of Fe with respect to pristine and discharged ones; the other discharged samples displayed similar spectra as the pristine sample, indicating that there were no obvious changes of Fe local environment during the insertion/extraction of Zn-ions. The pre-edge peaks of Fe at 7111.4 and 7114.2 eV are attributed to the $1s\rightarrow e_g$ and $1s\rightarrow t_{2g}$ electronic transitions of low-spin state Fe^{III}, and only C2 shows the 7111.4 eV peak as shown in Fig. 6(b). The FTs at Fe K-edges are shown in Fig. 6(d), based on the framework structure of MnHCF (-Fe-C-N-Mn-), the first two peaks are attributed to the carbon first shell (Fe-C) and nitrogen (Fe-C-N), while the third peak is related to manganese (Fe-C-N-Mn) [29]. The D10 sample shows a little different shape of the third peak with respect to other cycled sam-

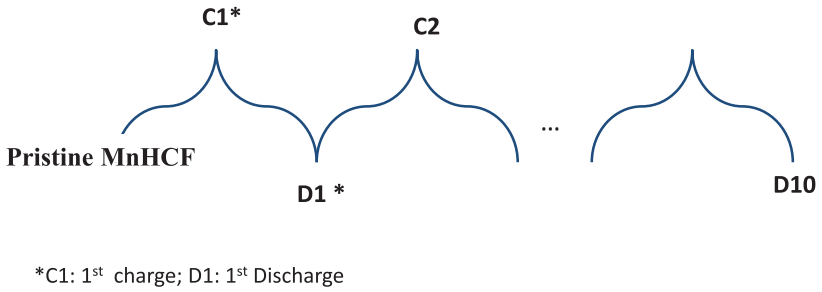

Fig. 5. Schematic diagram of samples of different charge/discharge states.

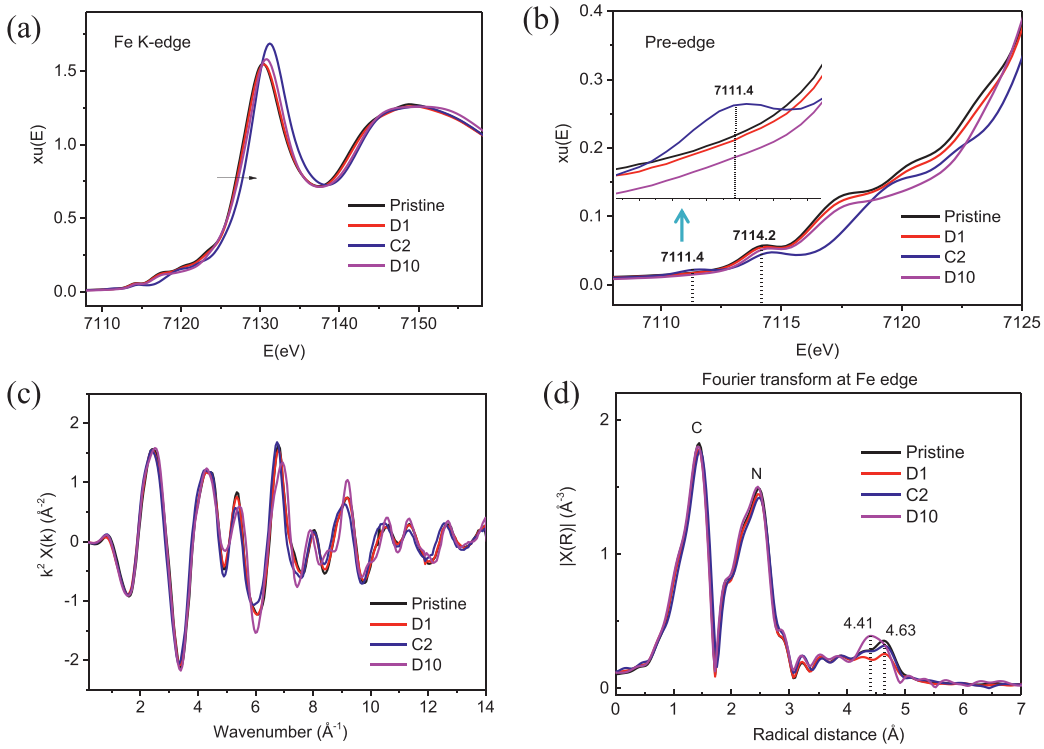

Fig. 6. (a) Ex-situ XANES of MnHCF powder and formulated electrodes at the Fe K-edge; (b) Zoom in the pre-edge feature of Fe K-edge; (c) k^2-weighted EXAFS signals and (d) corresponding Fourier transforms (FTs).

ples, which might reflect the Mn-Zn replacement during the insertion/extraction of Zn-ions.

Mn and Zn XANES K-edge spectra were recorded at same charge/discharge states (D1, C2 and D10) and are displayed in Fig. 7 (a,b) and (c,d), respectively. As well known, the rising edge portion of the XANES has a strong contribution from the 1 s to 4p transition, and factors that affect the shape and energy of selected features: oxidation state, coordination number and geometry, and covalency [40]. The pre-edge peaks (Fig. 7(c)) at 6540.3 eV and 6546.2 eV are considered to be the transition into T_{2g}/e_g and 4p orbitals in Mn^{2+}species, respectively. Overall, the spectra are nearly identical in both series of measurements. The only exception regards the D10 sample at the Mn K-edge, which displays a different curve shape. Therefore it is suggested that the local structure of manganese in pristine, D1, and C2 samples is similar and so does the local charge associated to the metal, because no obvious energy shift was observed. The different curve shape in D10 might be attributed to the change of local coordination and geometry with insertion/extraction of Zn-ions.

Table S2 displays the edge step values of Fe/Mn/Zn K-edge at the measured charge and discharge states, being these values related to the actual content of metal inside the electrode material. As indicated in the Table S2, the value for Fe K-edge shows almost no changes at D1, C2 and D10 states. However, the edge step value for Mn K-edge was reduced from pristine 0.215 to 0.00793 (D10), and this indicates that the Mn content inside the electrode was significantly decreased due to the dissolution. This was confirmed from the postmortem analysis of electrolyte (Table S3) in which Mn was detected inside the electrolyte after cycling. Thus, the low intensity of Mn K-edge at D10 state is related to the low Mn content inside the electrode.

The hypothesis of the Mn to Zn replacement is confirmed by looking at the XANES spectra at the Zn K-edge, showed in Fig. 7(b) (d). XANES spectra measure the transitions of electron from Zn 1 s to unoccupied 4p states, because the 3d orbitals are completely filled [41,42]. In order to have a reference to detect the local environment of Zn inside MnHCF structure, we synthesized the rhombohedral zinc hexacyanoferrate (ZnHCF). Surprisingly, all the samples show the same XANES spectra as ZnHCF, even the D1 and C2 samples, which indicates that even at the beginning of cycling, there is a formation of the ZnHCF phase inside the MnHCF structure. Where does the manganese go during the cycling? Elemental analysis conducted on the electrolyte solution bath as well as by using the edge step values of the measurements at both Mn and

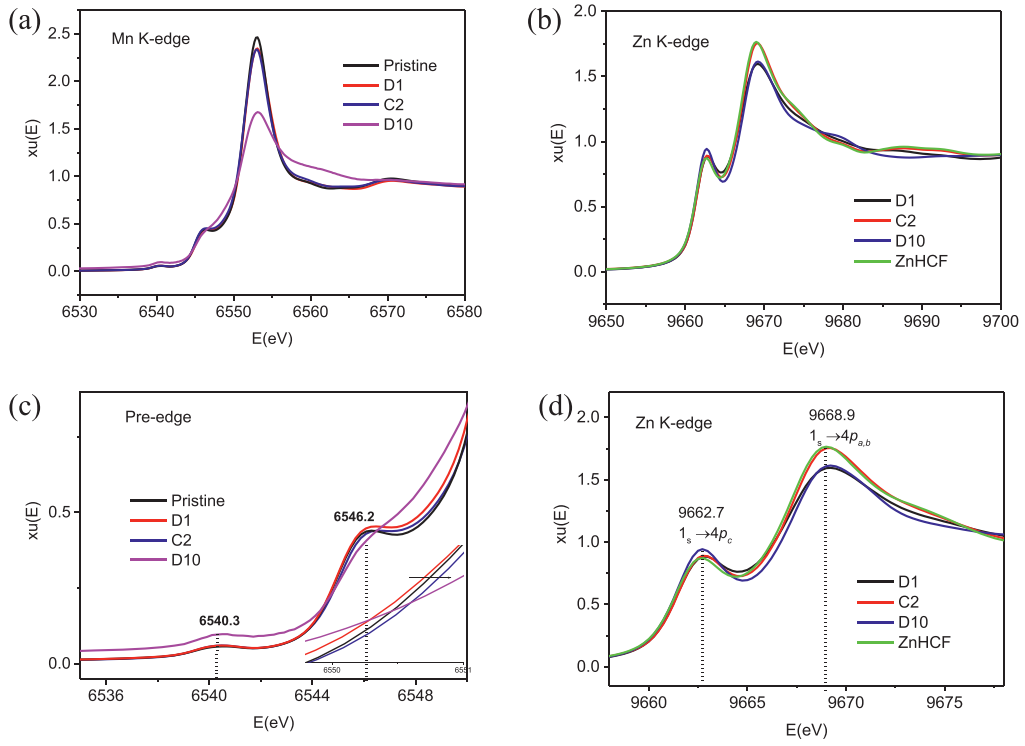

Fig. 7. (a) (b) Ex-situ XANES of MnHCF powder and formulated electrodes at the Mn and Zn K-edge; (c) pre-edge feature of Mn K-edge; (d) Zoom in the Zn K-edge.

Zn K-edge (Table S2), confirm dissolution of the Mn with concomitant enrichment of the Zn during cycling. A similar result was also reported by Li et al. [22], from ex-situ XPS spectra: Zn was not extracted completely at charged state, some residues exist in the MnHCF framework, and there is even a part of the Zn substituting the Mn-sites. Based on the edge step we got for the Zn K-edge at different charge/discharge states, there was residual Zn at the C2 state, and the value was increased from D1 to D10 (Table S2). The Corresponding FT's of k^2-weighted EXAFS signal of Mn K-edge and Zn K-edge (Fig. S1) show the same peak position for all the samples and the three peaks can be attributing to the nitrogen (Mn-N), carbon (Mn-N-C) and iron (Mn-N-C-Fe). Overall, from the XAS investigations, we can conclude that there is a part of Zn substitutiug Mn, forming the Zn-N-C-Fe structural framework, which is characteristic of the rhombohedral ZnHCF phase.

The stability of MnHCF fuel-cell was tested through both CV and galvanostatic charge/discharge, as shown in Fig. 8(a, b). The redox peaks from the 10th to the 50th cycle show a similar trend as the first 10 cycles,. The current intensity of the anode peak at around 1.7 V and two reduction peaks at 1.20–1.40 V are increasing within the first 30 cycles, and after that the current intensity reaches a stable state. Meanwhile, the reduction peak at 1.70–1.75 V keeps decreasing, and becomes stable after 30 cycles. Based on the report [43], the gradual activation of Fe-sites at the early cycles, can be attributed to the alleviation of spatial resistance with the dissolution of Mn-sites. But, with substitution by Zn-ions, the activation process was confined. The cycling performance of MnHCF at C/5 is shown in Fig. 8(b). The charge and discharge curves show an increasing trend from the 3rd∼20th cycle, and after 20cycles, the curve starts to decrease gradually. The discharge capacity is increased from 110 $mAhg^{-1}$ at 10th cycle, to around 115 $mAhg^{-1}$ at 20th cycle, and then decreased to 70 $mAhg^{-1}$ at 50th cycle. We found that the CV data is closely related to the galvanostatic charge and discharge data, and the peak current increasing or decreasing is reflected on the changing of capacity. Thus, from the data above, we can conclude that the activation of Fe-sites mainly happened during the first 20 cycles at C/5, and the decrease of the capacity can be related to the Zn-replacement of Mn-site inside the structure.

To confirm the low capacity of Zn-substituted MnHCF, the electrochemical performance of pure ZnHCF was investigated, as shown in Fig. 8(c, d). Contrary to the monoclinic structure of MnHCF, ZnHCF shows a rhombohedral structure (space group: R-3C) with a/b, c and γ equal to 12.5795(3) Å, 33.05134 (1) Å and 120°, respectively (Fig. S2 (a)). The CV curves of ZnHCF are stable and only one pair of redox peaks was observed at 1.94/1.71 V at 1 mV/s. The galvanostatic charge and discharge of ZnHCF at C/5 is shown in Fig. S2(b), with a discharge capacity of around 60 mAh g^{-1}, discharge plateau around 1.71 V. Cycling performance is shown in Fig. 8(d). The capacity fading was considerably fast, and only around 33% capacity was retained after 50cycles, due to the dissolution of ZnHCF, as suggested by Zhang et al. [16,44] and this also explains the capacity fading of MnHCF during cycling, as shown in Fig. 8(a, b).

4. Conclusion

The Electrochemical performance and electronic structure information of MnHCF were studied in aqueous Zn-ion batteries. From the cycling voltammetry and galvanostatic charge/discharge data, we found the gradual activation of Fe-sites and the deactivation of Mn-sites. The capacity contribution of Fe-sites increased from 30 to 86% during the first 10 cycles at C/20. The cycling stability of MnHCF was tested at C/5 for 50 cycles, and it shows an increasing capacity during the first 20 cycles, around 70% of capacity was retained after 50cycles. The activation of Fe-sites at the starting cycles can be attributed to the alleviation of spatial resistance, caused by the dissolution of Mn-sites. Based on the XAS analysis, the local environment of Fe-site didn't change a lot, while the Mn K-edge spectra had obvious changes at D10 state, and -Zn-NC-Fe- structure was detected in all the cycled samples. These results confirmed that there is partial replacement of Mn by Zn during

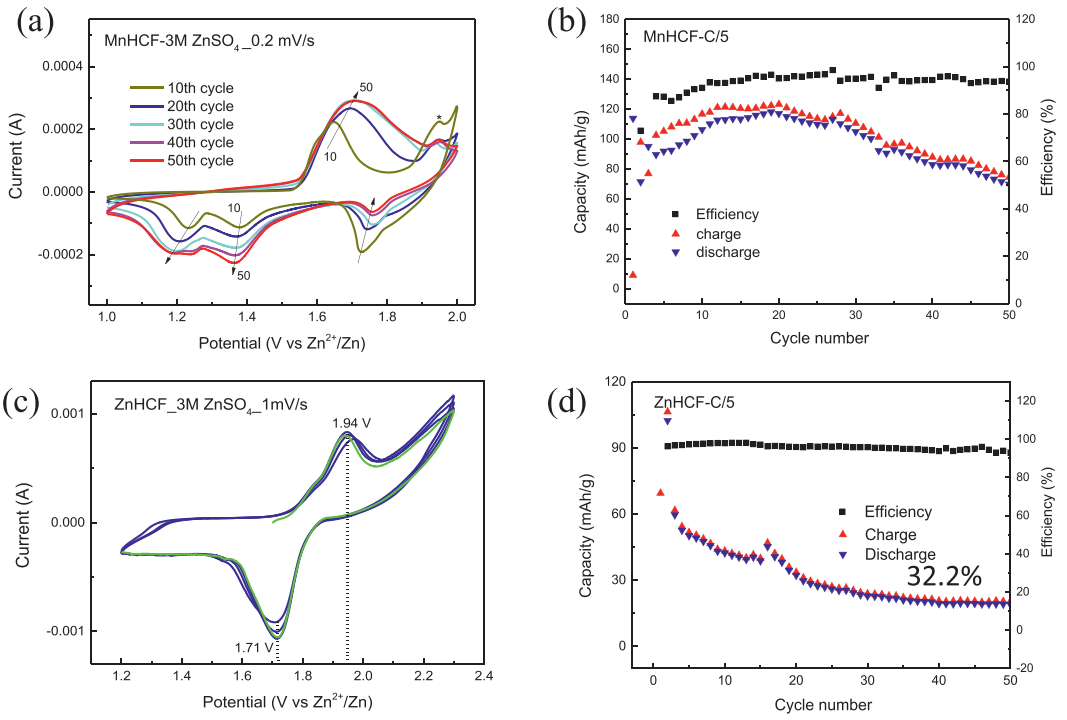

Fig. 8. (a) CV curves of MnHCF full-cell at 0.2 mV s^{-1} from 10th to 50th cycles; (b) cycling performance of MnHCF at C/5; (c) CV curve of ZnHCF at 1 mV/s; (d) cycling performance of ZnHCF at C/5 rate.

charge/discharge process, and this also explained the decreasing of capacity of MnHCF during the cycling.

Declaration of Competing Interest

The authors declare no conflict of interest.

Credit authorship contribution statement

Min Li: Methodology, Investigation, Data curation, Writing – original draft. **Rosalinda Sciacca:** Investigation, Writing – review & editing. **Mariam Maisuradze:** Investigation, Writing – review & editing. **Giuliana Aquilanti:** Investigation. **Jasper Plaisier:** Investigation. **Mario Berrettoni:** Supervision. **Marco Giorgetti:** Conceptualization, Methodology, Supervision, Project administration, Writing – review & editing.

Acknowledgements

Measurements at ELETTRA were supported by in-house research. This research was funded by the University of Bologna, RFO funding. M. Maisuradze acknowledges the support of CERIC-ERIC for providing the PhD bourse.

Supplementary materials

Supplementary material associated with this article can be found, in the online version, at doi:10.1016/j.electacta.2021.139414.

References

[1] W. Li, J.R. Dahn, D.S. Wainwright, Rechargeable lithium batteries with aqueous electrolytes, Science 264 (2016) 1115–1118.
[2] M.H. Lee, S.J. Kim, D. Chang, J. Kim, S. Moon, K. Oh, K.Y. Park, W.M. Seong, H. Park, G. Kwon, B. Lee, K. Kang, Toward a low-cost high-voltage sodium aqueous rechargeable battery, Mater. Today 29 (2019) 26–36, doi:10.1016/j.mattod.2019.02.004.
[3] L. Wang, Y. Lu, J. Liu, M. Xu, J. Cheng, D. Zhang, J.B. Goodenough, A superior low-cost cathode for a Na-Ion battery, Angew. Chem. Int. Ed. 52 (2013) 1964–1967, doi:10.1002/anie.201206854.
[4] A. Eftekhari, Potassium secondary cell based on Prussian blue cathode, J. Power Sources 126 (2004) 221–228, doi:10.1016/j.jpowsour.2003.08.007.
[5] Y. Mizuno, M. Okubo, E. Hosono, T. Kudo, K. Oh-Ishi, A. Okazawa, N. Kojima, R. Kurono, S.I. Nishimura, A. Yamada, Electrochemical Mg^{2+} intercalation into a bimetallic CuFe Prussian blue analog in aqueous electrolytes, J. Mater. Chem. A 1 (2013) 13055–13059, doi:10.1039/c3ta13205f.
[6] C. Xu, B. Li, H. Du, F. Kang, Energetic zinc ion chemistry: the rechargeable zinc ion battery, Angew. Chem. Int. Ed. 51 (2012) 933–935, doi:10.1002/anie.201106307.
[7] N. Kuperman, P. Padigi, G. Goncher, D. Evans, J. Thiebes, R. Solanki, High performance Prussian Blue cathode for nonaqueous Ca-ion intercalation battery, J. Power Sources 342 (2017) 414–418, doi:10.1016/j.jpowsour.2016.12.074.
[8] W.J. Li, S.L. Chou, J.Z. Wang, Y.M. Kang, J.L. Wang, Y. Liu, Q.F. Gu, H.K. Liu, S.X. Dou, Facile method to synthesize na-enriched Na1+xFeFe(CN)6 frameworks as cathode with superior electrochemical performance for sodium-ion batteries, Chem. Mater. 27 (2015) 1997–2003, doi:10.1021/cm504091z.
[9] Y. Hu, D. Ye, B. Luo, H. Hu, X. Zhu, S. Wang, L. Li, S. Peng, L. Wang, A binder-free and free-standing cobalt Sulfide@Carbon nanotube cathode material for Aluminum-ion batteries, Adv. Mater. 30 (2018) 1–6, doi:10.1002/adma.201703824.
[10] R. Trócoli, F.La Mantia, An aqueous zinc-ion battery based on copper hexacyanoferrate, ChemSusChem 8 (2015) 481–485, doi:10.1002/cssc.201403143.
[11] B. Tang, L. Shan, S. Liang, J. Zhou, Issues and opportunities facing aqueous zinc-ion batteries, Energy Environ. Sci. 12 (2019) 3288–3304, doi:10.1039/c9ee02526j.
[12] J. Shin, J. Lee, Y. Park, J.W. Choi, Aqueous zinc ion batteries: focus on zinc metal anodes, Chem. Sci. 11 (2020) 2028–2044, doi:10.1039/d0sc00022a.
[13] M. Giorgetti, L. Guadagnini, D. Tonelli, Structural characterization of electrodeposited copper hexacyanoferrate films by using a spectroscopic multitechnique approach, Phys. Chem. Chem. Phys. 14 (2012) 5527–5537, doi:10.1039/c2cp24109a.
[14] E. Caponetti, M. L. Saladino, P. Conti, D. Ranganathan, S. Zamponi, M. Berrettoni, M. Giorgetti, A. Zanotto, Synthesis and Characterization of Nanostructured Cobalt Hexacyanoferrate, J. Phys. Chem. C 114 (2010) 6401–6407, doi:10.1021/jp100367p.
[15] Z. Jia, B. Wang, Y. Wang, Copper hexacyanoferrate with a well-defined open framework as a positive electrode for aqueous zinc ion batteries, Mater. Chem. Phys. 149 (2015) 601–606, doi:10.1016/j.matchemphys.2014.11.014.
[16] L. Zhang, L. Chen, X. Zhou, Z. Liu, Towards high-voltage aqueous metal-ion batteries beyond 1.5 V: the zinc/zinc hexacyanoferrate system, Adv. Energy Mater. 5 (2015) 1–5, doi:10.1002/aenm.201400930.
[17] C. Wei, C. Xu, B. Li, H. Du, F. Kang, Preparation and characterization of manganese dioxides with nano-sized tunnel structures for zinc ion storage, J. Phys. Chem. Solids 73 (2012) 1487–1491, doi:10.1016/j.jpcs.2011.11.038.

[18] F. Wan, L. Zhang, X. Dai, X. Wang, Z. Niu, J. Chen, Aqueous rechargeable zinc/sodium vanadate batteries with enhanced performance from simultaneous insertion of dual carriers, Nat. Commun. 9 (2018) 1–11, doi:10.1038/s41467-018-04060-8.
[19] J. Zhou, L. Shan, Z. Wu, X. Guo, G. Fang, S. Liang, Investigation of V_2O_5 as a low-cost rechargeable aqueous zinc ion battery cathode, Chem. Commun. 54 (2018) 4457–4460, doi:10.1039/c8cc02250j.
[20] Z. Hou, X. Zhang, X. Li, Y. Zhu, J. Liang, Y. Qian, Surfactant widens the electrochemical window of an aqueous electrolyte for better rechargeable aqueous sodium/zinc battery, J. Mater. Chem. A 5 (2017) 730–738, doi:10.1039/c6ta08736a.
[21] Q. Li, K. Ma, G. Yang, C. Wang, High-voltage non-aqueous $Zn/K_{1.6}Mn_{1.2}Fe(CN)_6$ batteries with zero capacity loss in extremely long working duration, Energy Storage Mater. 29 (2020) 246–253, doi:10.1016/j.ensm.2020.04.030.
[22] W. Li, C. Xu, X. Zhang, M. Xia, Z. Yang, H. Yan, H. Yu, L. Zhang, W. Shu, J. Shu, Sodium manganese hexacyanoferrate as Zn ion host toward aqueous energy storage, J. Electroanal. Chem. 881 (2021), doi:10.1016/j.jelechem.2020.114968.
[23] L. Ma, S. Chen, C. Long, X. Li, Y. Zhao, Z. Liu, Z. Huang, B. Dong, J.A. Zapien, C. Zhi, Achieving high-voltage and high-capacity aqueous rechargeable Zinc ion battery by incorporating two-species redox reaction, Adv. Energy Mater. 9 (2019), doi:10.1002/aenm.201902446.
[24] Y. Zhang, Y. Wang, L. Lu, C. Sun, D.Y.W. Yu, Vanadium hexacyanoferrate with two redox active sites as cathode material for aqueous Zn-ion batteries, J. Power Sources 484 (2021) 229263, doi:10.1016/j.jpowsour.2020.229263.
[25] G. Kasiri, R. Trócoli, A. Bani Hashemi, F. La Mantia, An electrochemical investigation of the aging of copper hexacyanoferrate during the operation in zinc-ion batteries, Electrochim. Acta 222 (2016) 74–83, doi:10.1016/j.electacta.2016.10.155.
[26] R. Trócoli, G. Kasiri, F.La Mantia, Phase transformation of copper hexacyanoferrate ($KCuFe(CN)_6$) during zinc insertion: effect of co-ion intercalation, J. Power Sources 400 (2018) 167–171, doi:10.1016/j.jpowsour.2018.08.015.
[27] J. Lim, G. Kasiri, R. Sahu, K. Schweinar, K. Hengge, D. Raabe, F.La Mantia, C. Scheu, Irreversible structural changes of copper hexacyanoferrate used as a cathode in Zn-ion batteries, Chem. A Eur. J. 26 (2020) 4917–4922, doi:10.1002/chem.201905384.
[28] V. Renman, D.O. Ojwang, M. Valvo, C.P. Gómez, T. Gustafsson, G. Svensson, Structural-electrochemical relations in the aqueous copper hexacyanoferrate-zinc system examined by synchrotron X-ray diffraction, J. Power Sources 369 (2017) 146–153, doi:10.1016/j.jpowsour.2017.09.079.
[29] A. Mullaliu, J. Asenbauer, G. Aquilanti, S. Passerini, M. Giorgetti, Highlighting the reversible manganese electroactivity in Na-rich manganese hexacyanoferrate material for Li- and Na-ion storage, Small Methods 4 (2020), doi:10.1002/smtd.201900529.
[30] J.R. Plaisier, L. Nodari, L. Gigli, E.P.R.S. Miguel, R. Bertoncello, A. Lausi, The X-ray diffraction beamline MCX at Elettra: a case study of non-destructive analysis on stained glass, Acta IMEKO 6 (2017) 71–75, doi:10.21014/acta_imeko.v6i3.464.
[31] J. Rodríguez-Carvajal, Recent advances in magnetic structure determination by neutron powder diffraction, Phys. B Phys. Condens. Matter. 192 (1993) 55–69, doi:10.1016/0921-4526(93)90108-I.
[32] G. Aquilanti, M. Giorgetti, R. Dominko, L. Stievano, I. Arčon, N. Novello, L. Olivi, Operando characterization of batteries using x-ray absorption spectroscopy: advances at the beamline XAFS at synchrotron Elettra, J. Phys. D. Appl. Phys. 50 (2017), doi:10.1088/1361-6463/aa519a.
[33] M. Newville, A. Ifeffit, HEPHAESTUS: data analysis for X-ray absorption spectroscopy, J. Synchrotron Rad. 12 (2005) 537–541, doi:10.1107/S0909049505012719.
[34] S.J. Gerber, E. Erasmus, Electronic effects of metal hexacyanoferrates : an XPS and FTIR study, Mater. Chem. Phys. 203 (2018) 73–81, doi:10.1016/j.matchemphys.2017.09.029.
[35] D.O. Ojwang, J. Grins, D. Wardecki, M. Valvo, V. Renman, L. Häggström, T. Ericsson, T. Gustafsson, A. Mahmoud, P. Hermann, G. Svensson, Structure characterization and properties of K-containing copper hexacyanoferrate, Inorg. Chem. 12 (2016) 5924–5934, doi:10.1021/acs.inorgchem.6b00227.
[36] M.A. Oliver-Tolentino, J. Vázquez-Samperio, S.N. Arellano-Ahumada, A. Guzmán-Vargas, D. Ramírez-Rosales, J.A. Wang, E. Reguera, Enhancement of stability by positive disruptive effect on Mn-Fe charge transfer in vacancy-free Mn-Co hexacyanoferrate through a charge/discharge process in aqueous Na-ion batteries, J. Phys. Chem. C 122 (2018) 20602–20610, doi:10.1021/acs.jpcc.8b05506.
[37] M.H. Alfaruqi, V. Mathew, J. Gim, S. Kim, J. Song, J.P. Baboo, S.H. Choi, J. Kim, Electrochemically induced structural transformation in a γ-MnO_2 cathode of a high capacity zinc-ion battery system, Chem. Mater. 27 (2015) 3609–3620, doi:10.1021/cm504717p.
[38] N. Zhang, F. Cheng, Y. Liu, Q. Zhao, K. Lei, C. Chen, X. Liu, J. Chen, Cation-deficient spinel $ZnMn_2O_4$ Cathode in $Zn(CF_3SO_3)_2$ electrolyte for rechargeable aqueous zn-ion battery, J. Am. Chem. Soc. 138 (2016) 12894–12901, doi:10.1021/jacs.6b05958.
[39] Q. Yang, F. Mo, Z. Liu, L. Ma, X. Li, D. Fang, S. Chen, S. Zhang, C. Zhi, Activating C-coordinated iron of iron hexacyanoferrate for Zn hybrid-ion batteries with 10 000-cycle lifespan and superior rate capability, Adv. Mater. 31 (2019) 1–9, doi:10.1002/adma.201901521.
[40] M. Giorgetti, A review on the structural studies of batteries and host materials by X-ray absorption spectroscopy, Int. Sch. Res. Not. 2013 (2013) 22 Article ID 938625, doi:10.1155/2013/938625.
[41] E.Y.M. Lee, N. Tran, J. Russell, R.N. Lamb, Nanocrystalline order of zinc oxide thin films grown on optical fibers, J. Appl. Phys. 92 (2002) 2996–2999, doi:10.1063/1.1495064.
[42] J. Haug, A. Chassé, M. Dubiel, C. Eisenschmidt, M. Khalid, P. Esquinazi, Characterization of lattice defects by X-ray absorption spectroscopy at the Zn K-edge in ferromagnetic, pure ZnO films, J. Appl. Phys. 110 (2011), doi:10.1063/1.3631774.
[43] Q. Yang, F. Mo, Z. Liu, L. Ma, X. Li, D. Fang, S. Chen, S. Zhang, C. Zhi, Activating C-coordinated iron of iron hexacyanoferrate for Zn Hybrid-ion batteries with 10 000-cycle lifespan and superior rate capability, Adv. Mater. 31 (2019) 0–17, doi:10.1002/adma.201901521.
[44] G. Ni, B. Han, Q. Li, Z. Ji, B. Huang, C. Zhou, Instability of Zinc hexacyanoferrate electrode in an aqueous environment: redox-induced phase transition, compound dissolution, and inhibition, ChemElectroChem 3 (2016) 798–804, doi:10.1002/celc.201500538.